Combined experimental-computational study to discrete fracture of brittle materials

K. De Proft[1], G.N. Wells[2], L.J. Sluys[2] and W.P. De Wilde[1].

[1]   Department of Mechanics of Materials and Constructions
      Vrije Universiteit Brussel
      Pleinlaan 2, 1050 Brussels, Belgium.
[2]   Faculty of Civil Engineering and Geosciences
      Delft University of Technology
      Stevinweg 1, 2628 CN, Delft, The Netherlands.

In this paper, a combined experimental-computational study of a double-edge notched specimen subjected to tensile loading is presented. In the experimental part, the load-deformation response and the displacement field around the crack tip are recorded. An Electronic Speckle Pattern Interferometer (ESPI) is used to obtain the local displacement field. The experimental results are used to validate a numerical model for the description of fracture using finite elements. The numerical model uses displacement discontinuities to model cracks. The discontinuities are able to pass through finite elements. At the discontinuity, a plasticity-based and a combined damage-plasticity cohesive zone model are used, while the continuum remains elastic. Both local and global results from the numerical simulations are compared with experimental data.

Key words: Discontinuous model, monotonic and cyclic loading, ESPI

1   Introduction

A variety of computational techniques exists to describe the fracture behaviour of quasi-brittle materials. These numerical models must be able to simulate the behaviour of brittle materials under different loading conditions. Therefore, experimental data is very important. Firstly, experimental data is needed in order to determine if the proposed numerical models are capable of simulating the observed behaviour. Secondly, experimental data are necessary to obtain model parameters. Conversely, numerical simulations can be used to improve experiments by a simultaneous experimental/computational study. Clearly, the link between experimental and computational work is extremely important.

In this paper, the combined experimental-computational study of a double-edge notched (DEN) stone specimen subjected to tensile loading is presented. In the first section, the experimental set-up is presented and experimental results are discussed. Monotonic as well as cyclic loading condi-

tions are considered. Then, a discontinuous finite element formulation based on partitions of unity in combination with a plasticity-based and a combined damage-plasticity cohesive zone law are introduced for the simulation of the DEN-tensile tests. Finally, the numerical results are compared with experimental data.

2   Experimantal set-up

For the experiments, a natural stone (limestone) named 'Massangis' is used. Nowadays, this type of limestone is frequently used for renovation purposes. The natural stone *Massangis* is available in several varieties and is exploited in Massangis, France. The variety '*Massangis Roche Jaune*' is used for the experiments.

All specimens are 120 mm high and 50 mm wide. The thickness is 11 mm. Notches 7 mm deep and 1 mm wide are sawn in the middle of both sides of the specimen. The geometry of the specimen is shown in figure 1. Two Linear Variable Differential Transducers (LVDT) are used for the measurement of the deformation. The LVDT's are placed over the notches on each side of the specimen, as indicated in figure 1. The vertical measuring range of the LVDT's is 20 mm. Due to the notches, the crack will be located within the range of the LVDT's. When a macro crack starts to grow, the deformations tend to localize in the cracked area. Other parts of the specimen will unload. When the crack is not in the range of the LVDT's or when the measuring range of the LVDT's is too large a snap back will occur, making the measurement of the post peak behaviour impossible. In the other
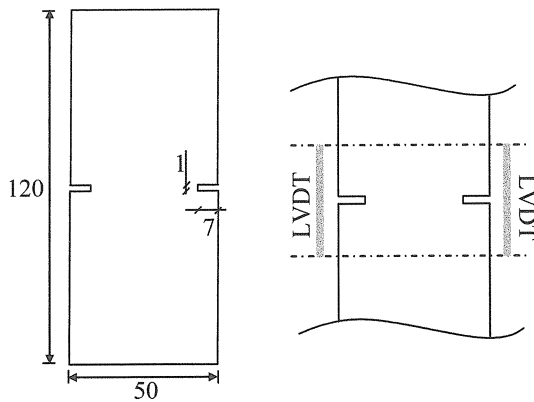

Figure 1: Geometry of the specimen (all dimensions in mm) and placement of LVDT.

case, when the crack is situated in the range of the LVDT's, the measured deformation increases gradually. In this case, the average signal of the LVDT's can be used as the control signal for the test. The average signal is also used in the load-deformation response.

The experiments are performed with an INSTRON 4505 testing bench. The specimens are directly glued to the loading platens, so that the boundaries of the specimen cannot rotate. Tensile loading is applied by means of a uniform vertical displacement of the boundary. For the cyclic loading cases, two unloading-reloading sequences are carried out in the post peak regime. All tests were performed under displacement control at a rate of 0.3 μm/s.

An Electronic Speckle Pattern Interferometer (ESPI) device is used to record the local displacement field at different load steps. The specimen is illuminated by laser light and speckles appear on the lighted surface. A CCD camera captures the reflected light. The observed speckle pattern includes information about the deformation of the specimen. By subtracting different speckle patterns, interference fringes are formed. These fringes contain information about the displacement of the studied specimen. Unlike strain gauges, there is no contact with the studied specimen and the strain field, which can be computed with the supplied software, of a section of the specimen can be studied. A user-defined border restricts the measuring area of the ESPI. Within this border, a reference point is defined. This reference point is assumed not to move and the displacements of all material points situated inside the border are referred to the reference point. In order to make a comparison with numerical results, five paths are defined along which the displacements are monitored at several load steps. The different load paths and the position of the reference point are shown in figure 2. Subtracting the displacements in y-direction along path 1 from the corresponding displacements along path 2 results in the deformation between those two paths.
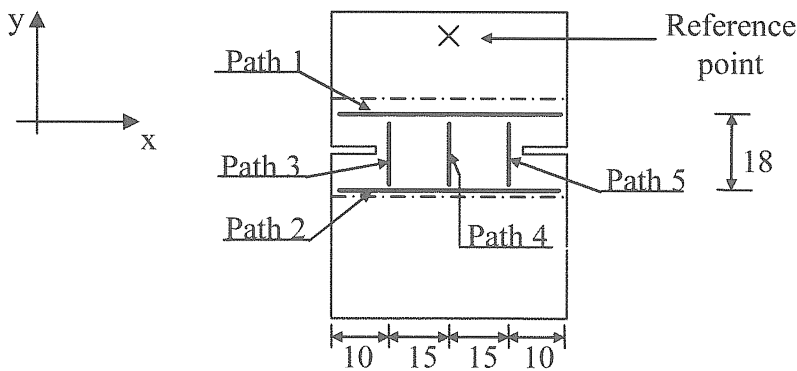

Figure 2: Position of the reference point and paths for ESPI measurement.

3   Experimental results

3.1 Monotonic loading
A typical load-deformation curve is shown in figure 3. The behaviour is nearly linear elastic until the peak load. Just before peak load, the curve deviates slightly from the linear elastic branch. This indicates that some micro-cracking is occurring before the peak load has been reached. After the peak load, a sharp drop is observed, indicating a brittle response. At this stage, deformation is localized in a single macro crack and the behaviour is highly non-linear. Apart from the load-deformation curve, also the displacement field in the vicinity of the crack tip is measured. Black dots (in figure 3) represent load levels where snapshots of the displacement field within the defined border are taken. The deformations for various load levels, measured in the y-direction between path 1 and 2 are shown in figure 4a. For load level I, the deformations are approximately uniform. For all
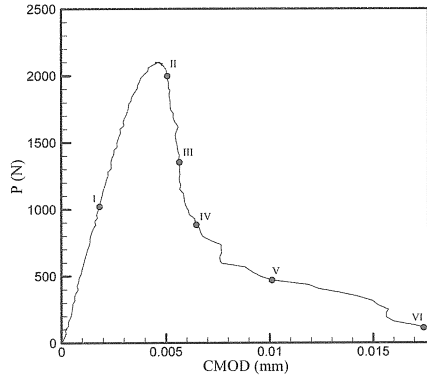
Figure 3: Representative load-deformation curve for monotonic loaded specimen.
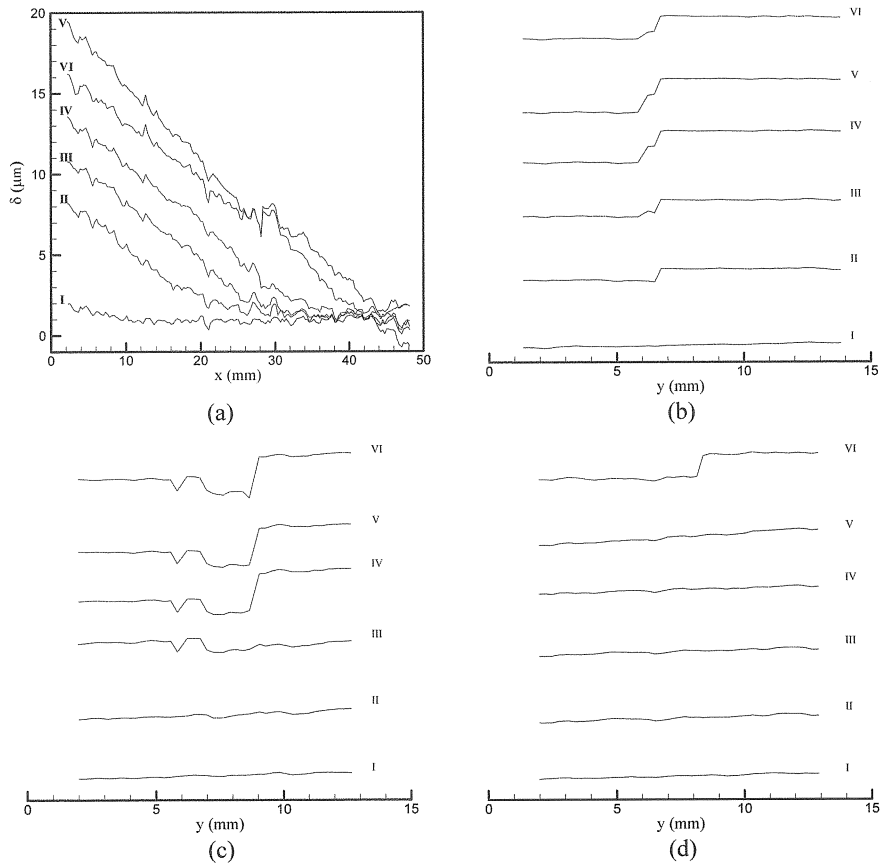

(a)

(b)

(c)

(d)

Figure 4: (a) Deformations measured between path 1 and path 2, (b) displacements along path 3, (c) path 4 and (d) path 5 referred to the reference point.

other load levels, the obtained deformations are highly non-uniform, indicating crack growth from the left to the right notch. The location of the crack tip during loading can be followed with the deformations. Near load level VI, the crack has crossed the complete specimen. Figures 4b-d show the displacements measured along path 3, 4 and 5. The represented values are relative to the reference point and consequently, no quantitative conclusions can be made. Therefore, no vertical axis is shown. The shown profiles are valid for the subsequent load levels. Nevertheless, the results are very useful. As can be seen, the crack which started at the left notch resulting in a jump in the displacements along path 3 (figure 4b). In the middle of the specimen (figure 4c) and at the right notch (figure 4d), the displacements are still continuous. At load level IV, the crack has reached the centre of the specimen, while the crack has crossed the entire specimen at load level VI.

From the shown profiles (figure 4b-d), the magnitude of the displacement jump can be computed. Again, by computing the relative difference, the influence of the reference point is eliminated. Figure 5 shows the evolution of the crack opening on the left side (squares), the middle (triangles) and the right side (circles) of the specimen as a function of the load level. The crack opening measured at the left notch first increases. At load level IV, a crack opening in the middle of the specimen is measured. Finally, at load level VI, the crack has reached the right notch. At this time, the crack opening at the left notch decreases again. This can also be observed in figure 4.a, where the deformation profile for load level VI is situated under the deformation profile for level V. Although the deformation profile at load level VI, shown in figure 4a, was not uniform, a tendency towards uniform deformations can be noticed.
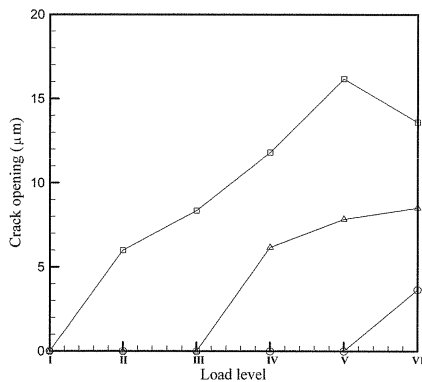

Figure 5: Crack opening at right notch (circles), left notch (squares) and middle notch (triangles) for different load levels.

3.2 Cyclic loading

Besides monotonic loading, DEN specimens were also subjected to cyclic loading. In all tests, two unloading cycles were introduced. A typical load-deformation response is shown in figure 6.
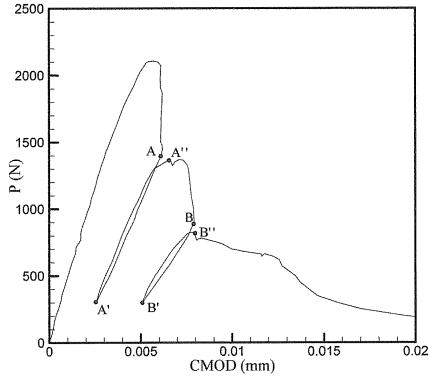
Figure 6: Load-deformation curve for cyclic loaded specimen.

Examining the load-deformation curve, three issues should be emphasized:

- after complete unloading, the closure of the crack is not complete;
- the unloading stiffness reduces with increasing deformation; and
- during the unloading/loading cycle, a small amount of energy is dissipated.

Black dots represent points where a snapshot of the displacement field is taken. The displacements along the predefined paths are extracted from the measurements. Only snapshots before and after unloading are shown.

Again, the deformation between path 1 and path 2 is computed in order to remove the influence of the reference point. Figure 7a shows the deformations before (A) and after (A') unloading and after reloading (A''). It is clear that before unloading, a crack is growing from the right notch. As was the
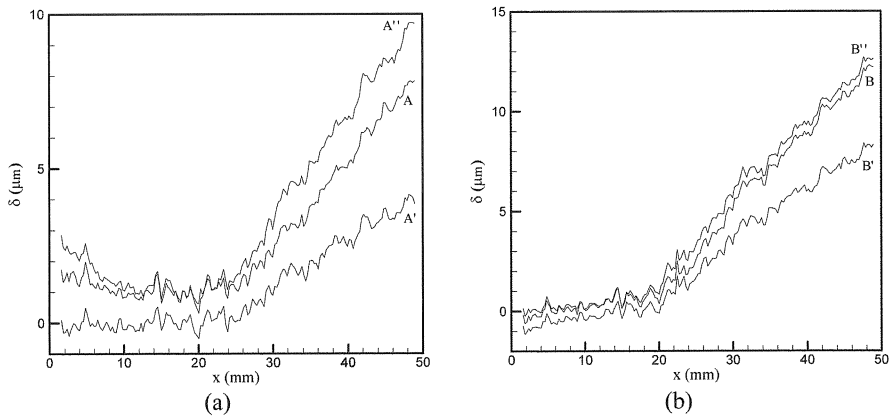

Figure 7: Deformations before and after unloading and after reloading for (a) the first cycle and (b) the second cycle.

228

case for monotonic loading, the deformations are highly non-uniform. Then, the tensile loading is decreased until *P = 300 N*. When the deformations obtained after unloading are studied (figure 7a – A'), it is clear that the specimen is divided into two parts:

- a first part where deformations are vanishing when the load is decreasing, indicating elastic or damage behaviour;
- a second part where, after unloading, permanent deformations occur.

After reloading (figure 7a – A''), the deformations recover to approximately the same values as before unloading (note that the difference between A and A'' in figure 7a is due to the difference in CMOD when the snapshot was taken). The loading-unloading-reloading cycle is repeated further in the post peak branch. Examining figure 7b, the same conclusions can be drawn. Note that the permanent deformations after unloading have increased, compared with the first cycle (compare A' in figure 7a with B' in figure 7b).

Displacements along path 5 (see figure 2) are shown in figure 8. The values are referred to the reference point and are only used for an indication of the evolutions of the displacement jumps. From figure 8a-b, it is clear that after unloading the crack does not completely close.
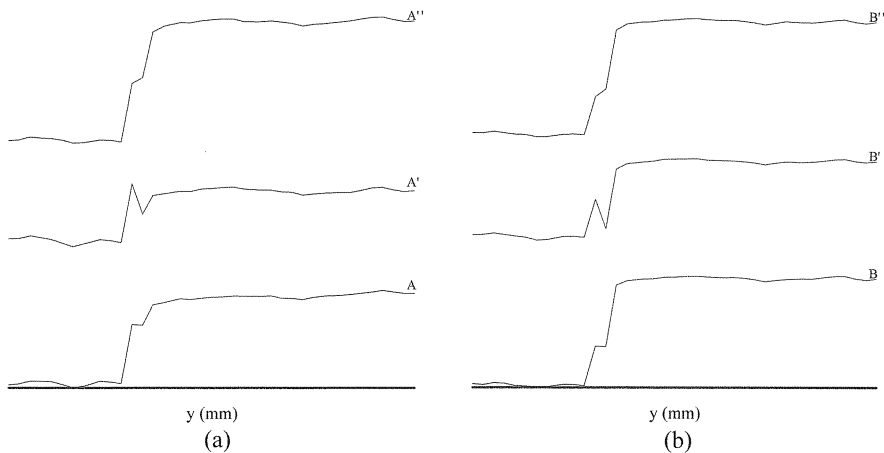

y (mm)　　　　　　　　　　y (mm)

(a)　　　　　　　　　　(b)

Figure 8: Evolution of the displacements along path 5 for (a) the first cycle and (b) the second cycle.

4　Numerical model

4.1 Discontinuous finite elements based on partitions of unity

A discontinuous model is used for the description of fracture within finite elements. Therefore, discontinuous modes are inserted into the approximation basis. Consequently, discontinuities are able to propagate through the finite element mesh, which is a very important advantage over interface elements, which allow discontinuities to propagate only along element boundaries. For a discontinuous displacement, it can be decomposed as:

$$\mathbf{u} = \hat{\mathbf{u}} + \sum_{i=1}^{m} \mathsf{H}_{\Gamma_i} \widetilde{\mathbf{u}}_i \qquad (1)$$

where $\mathbf{u}$ is the displacement field of a body Ω crossed by m non-intersecting discontinuities Γ_i, $\hat{\mathbf{u}}$ and $\widetilde{\mathbf{u}}$ are continuous fields and H_{Γ_i} is the Heaviside step function. Figure 9 shows a body crossed by two discontinuities. The displacement field can be interpolated as:

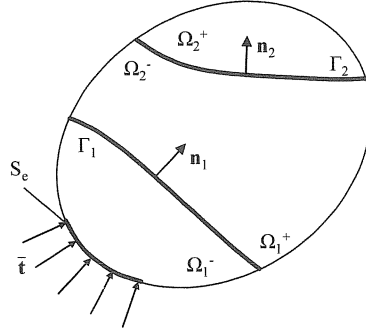$$\mathbf{u} = \mathbf{N}\mathbf{a} + \sum_{i=1}^{m} \mathsf{H}_{\Gamma_i} \mathbf{N}\mathbf{b}_i \qquad (2)$$

Figure 9: Body crossed by two discontinuities.

where $\mathbf{N}$ is the matrix containing the finite element shape functions, a are the 'regular' degrees of freedom and $\mathbf{b}_i$ are the 'enhanced' degrees of freedom related to crack i. For each crack, an additional set of degrees of freedom are added. The resulting linearized governing equations can be expressed as:

$$\begin{bmatrix} \mathbf{K}_{aa} & \mathbf{K}_{ab_1} & \cdots & \mathbf{K}_{ab_m} \\ \mathbf{K}_{b_1 a} & \mathbf{K}_{b_1 b_1} & \cdots & \mathbf{K}_{b_1 b_m} \\ \vdots & \vdots & \vdots & \vdots \\ \mathbf{K}_{b_m a} & \mathbf{K}_{b_m b_1} & \cdots & \mathbf{K}_{b_m b_m} \end{bmatrix} \begin{Bmatrix} d\mathbf{a} \\ d\mathbf{b}_1 \\ \vdots \\ d\mathbf{b}_m \end{Bmatrix} = \begin{Bmatrix} \mathbf{f}_a^{\text{ext},t+\Delta t} \\ 0 \\ \vdots \\ 0 \end{Bmatrix} - \begin{Bmatrix} \mathbf{f}_a^{\text{int},t} \\ \mathbf{f}_{b_1}^{\text{int},t} \\ \vdots \\ \mathbf{f}_{b_m}^{\text{int},t} \end{Bmatrix} \qquad (3)$$

where

$$\mathbf{K}_{aa} = \int_{\Omega} \mathbf{B}^T \mathbf{C}^e \mathbf{B} d\Omega$$

$$\mathbf{K}_{ab_j} = \int_{\Omega} \mathsf{H}_{\Gamma_j} \mathbf{B}^T \mathbf{C}^e \mathbf{B} d\Omega$$

$$\mathbf{K}_{b_j a} = \int_{\Omega} \mathsf{H}_{\Gamma_j} \mathbf{B}^T \mathbf{C}^e \mathbf{B} d\Omega \qquad (4)$$

$$\mathbf{K}_{b_i b_j} = \int_{\Omega} \mathsf{H}_{\Gamma_i} \mathsf{H}_{\Gamma_j} \mathbf{B}^T \mathbf{C}^e \mathbf{B} d\Omega$$

$$\mathbf{K}_{b_j b_j} = \int_{\Omega} \mathsf{H}_{\Gamma_j} \mathbf{B}^T \mathbf{C}^e \mathbf{B} d\Omega + \int_{\Gamma_j} \mathbf{N}^T \mathbf{D} \mathbf{N} d\Gamma_j$$

where $\mathbf{C}^e$ is the elastic continuum material tensor and $\mathbf{D}$ is the material tangent for the discontinuity. It can be seen from equations (4) that the global system of equations remains symmetric when $\mathbf{C}^e$ and $\mathbf{D}$ are symmetric. Note that all stiffness contributions in equations (4) are very similar. The

crucial difference between the terms in equation (4) is the presence of the Heaviside function. This makes the finite element implementation relatively simple. It is assumed that the considered element is crossed by discontinuity *j* and influenced by discontinuity *i*. Detailed information on the discontinuity model can be found in Wells (2001) and De Pr oft (2003).

4.2 A plasticity based cohesive zone model

The behaviour within the discontinuity is described by a plasticity based cohesive zone model. The adopted plasticity model was proposed by Carol et al. (1997) for use in interface elements. Consequently, the plastic yield function is given in the traction space. A hyperbolic yield surface is introduced according to

$$f = T_t^2 - \left(c - T_n \tan \phi\right)^2 + \left(c - f_t \tan \phi\right)^2 \tag{5}$$

where $\mathbb{T} = \{T_n, T_t\}$ are the normal and tangential component of the traction vector, c is the cohesion, f_t the tensile strength and ϕ the internal friction angle of the material. For tension, an associative flow rule is adopted. The evolution of the yield surface is governed by the decrease in tensile strength and cohesion throughout the computation:

$$f_t = f_{t0}\left(1 - \frac{W_{cr}}{G_I^f}\right) \tag{6a}$$

$$c = c_0\left(1 - \frac{W_{cr}}{G_{II}^f}\right) \tag{6b}$$

where f_{t0} and c_0 are the initial values for the tensile strength and the cohesion, G_I^f is the mode-I fracture energy, G_{II}^f is the mode-II fracture energy and W_{cr} is the energy dissipated in the fracture processes. The incremented dissipated energy is defined as:

$$dW_{cr} = T_n d\Delta_n^{pl} + T_t d\Delta_t^{pl} \tag{7a}$$

and

$$W_{cr} = \int_0^t dW_{cr} \tag{7b}$$

where $\Delta = \{\Delta_n^{pl}, \Delta_t^{pl}\}$ are the normal and tangential component of the plastic separation vector. In this way, the decrease of tensile strength and cohesion is coupled to the energy dissipated during the fracture processes. Moreover, the choice of equation 6 ensures that the total mode-I fracture energy/mode-II fracture energy is dissipated when the tensile strength/cohesion vanishes. Furthermore, the decrease in tensile strength and cohesion is coupled; when a material is damaged due to tensile loading, the tensile strength and the cohesion decrease.

The tangential stiffness and the stress update are obtained with classical elasto-plastic equations. However, the elastic stiffness is chosen very high (in theory infinite) in order to suppress the artificial elastic part of the solution. Since a discontinuity is only inserted when the yield condition is violated, and the jump is completely inelastic.

4.3 A combined damage-plasticity cohesive zone model

In order to model the decrease in unloading stiffness and the accumulation of permanent deformations, a combined damage-plasticity model is used. The model is degenerated from the continuum case (De Proft, 2003), resulting in

$$\mathbf{T} = (1 - \omega)\, \mathbf{Q}^e \left(\mathbf{\Delta} - \mathbf{\Delta}^{pl} \right) \tag{8}$$

where $\mathbf{T}$ is the traction vector as defined before, ω is the degenerated damage variable, $\mathbf{Q}^e$ is the elastic acoustic tensor and $\mathbf{\Delta}^{pl}$ and $\mathbf{\Delta}$ are the plastic and total separation vector, respectively. The elastic acoustic tensor is defined as:

$$\mathbf{Q}^e = \mathbf{n}\,\mathbf{C}^e\,\mathbf{n} \tag{9}$$

Equation (8) is very similar to the constitutive equation used in continuum problems (Simo & Ju, 1987). The degenerated damage variable ω is analogous to the continuum damage variable. However, the degenerated damage variable ω varies from –infinity to 1. The elastic material tensor is replaced by the elastic acoustic tensor. A major difference with continuum models is that the elastic part has disappeared in the degenerated model, so that the separation of the discontinuity is completely inelastic. The separation is decomposed into a damage (recoverable) part and into a plastic (irrecoverable) part.

The plasticity model is solved in the effective traction space. The adopted yield surface is

$$f^p = \hat{T}_n - H\kappa^p \tag{10}$$

where $\hat{T}_n$ is the effective normal traction, H is the hardening/softening modulus and κ^p is the internal plastic variable. The evolution of damage is coupled to the damage loading function. This function is written in terms of an equivalent strain measure. However, strains are not defined in the discontinuity, so a new equivalent strain measure must be found. Analogous to the positive principal strain measure, the positive normal separation opening is used, resulting in

$$f^d = \Delta_n - \overline{\kappa}^d \tag{11}$$

where Δ_n is the normal separation of the discontinuity and $\overline{\kappa}^d$ is the degenerated internal damage variable. When the damage loading function is violated, the degenerated damage variable is updated via

$$\omega = 1 - \frac{\kappa_i}{\overline{\kappa}^d}\exp\left[-\beta\overline{\kappa}^d\right] \tag{12}$$

where κ_i is the damage threshold and β is a model parameter.

5   Numerical simulations vs experimental results

In this section, numerical simulations performed with the embedded discontinuities based on the partitions of unity. A quadratic six-noded triangular element is used as underlying finite element. The mesh independency of this solution has already been discussed in Wells and Sluys (2001) and De Proft (2003).

5.1 Monotonic loading

The simulations for the monotonic loading cases are performed with the plasticity-based cohesive zone model presented in section 4.2. For the first simulation, the following model parameters are adopted: $f_t = 6.2$ MPa, $c = 20$ MPa, $\phi = 26.35°$, $G_{fI} = 0.04$ N/mm and $G_{fII} = 0.1$ N/mm.
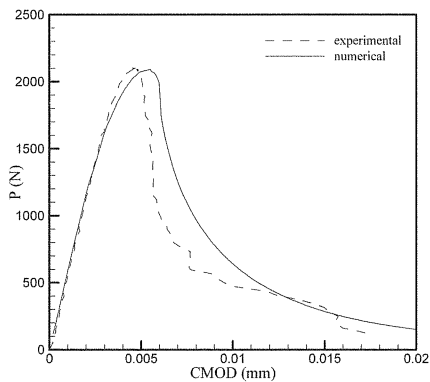
Figure 10: Experimental and numerical load-deformation curve.

The computed load-deformation curve is shown in figure 10. As can be seen, a good fit between numerical simulations and experimental results is obtained. The numerical curve deviates slightly before the peak load, compared with the experimental curve. Furthermore, the experimental post peak behaviour is more brittle. The peak load is captured well. Apart from the global response, the growth of the crack and the displacements in the fracture zone should be considered. Figure 11a-d compares the experimental deformation profiles captured at different load levels with the numerically obtained values. The deformations are computed from the displacement values obtained for path 1 and path 2.

Figure 11a shows the deformation profile in the elastic stage. The numerical simulation is perfectly symmetric and shows a good agreement with measured deformations. Figure 11b is a snapshot just after peak load. Clearly, the experimental deformation profile shows asymmetric crack growth while for the numerical simulation the profile remains symmetric. In figure 11c-d, the asymmetry in the experimental result increases, while the numerical simulations return to a uniform situation. Clearly, the model is not able to capture the correct experimental observations. The symmetric crack growth is a logical solution since the geometry and the test set-up are completely symmetric. The numerical model needs to be enhanced in order to capture the experimentally observed defor-
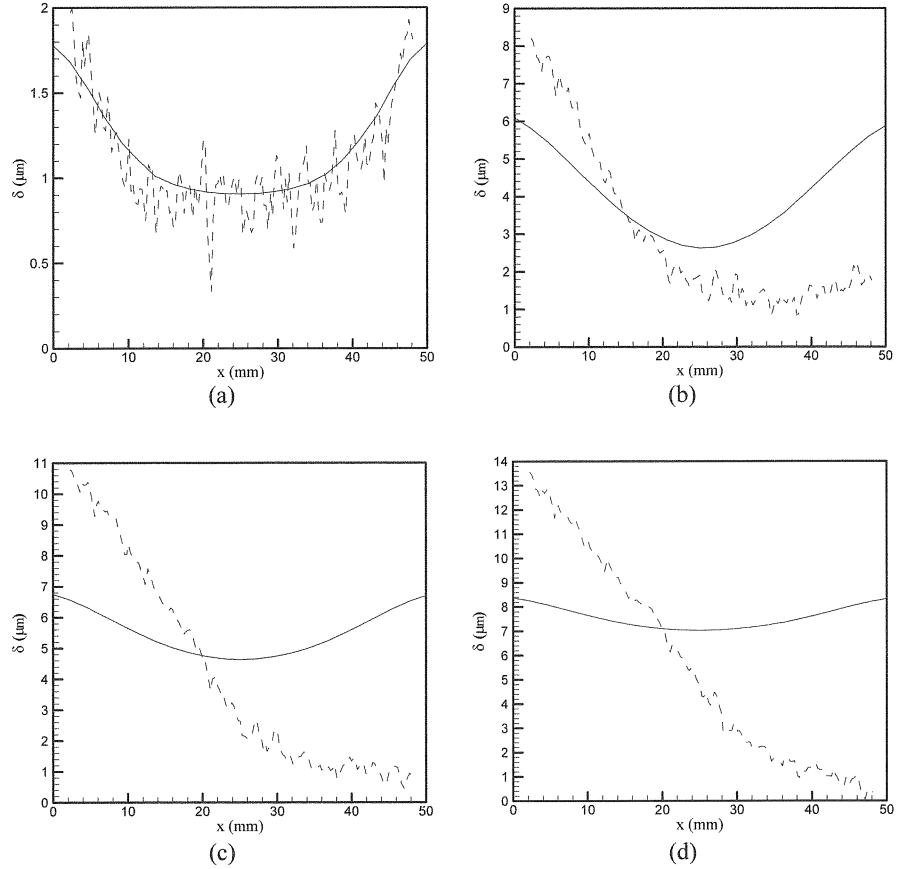
Figure 11: Deformation profiles at (a) load level I, (b) load level II, (c) load level III and (d) load level IV (solid lines represent numerical results).

mations. Non-symmetric crack growth can be numerically triggered by:

- introducing a weaker spot at a notch so that the crack starts earlier; or
- introducing bending, resulting in a non-uniform stress state.

Firstly, an element at the left notch is made slightly weaker. The tensile strength is decreased by 5%. Consequently, the cracks starts earlier in this element and crack propagation may be non-symmetric. The model parameters are: $f_t = 6.7$ MPa, $c = 20$ MPa, $\phi = 26.35°$, $G_{fI} = 0.03$ N/mm and $G_{fII} = 0.1$ N/mm. The obtained load-deformation curve is shown in figure 12. Examining figure 12, two remarks can be made:

- the peak load is captured correctly; and
- just after the peak load, the computed post peak behaviour is more ductile. Around load level P = 1350 N, a drop in the load-deformation curve is observed. After the drop, the computed post peak behaviour is close to the measured curve.
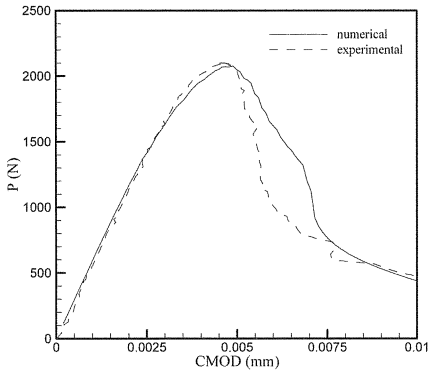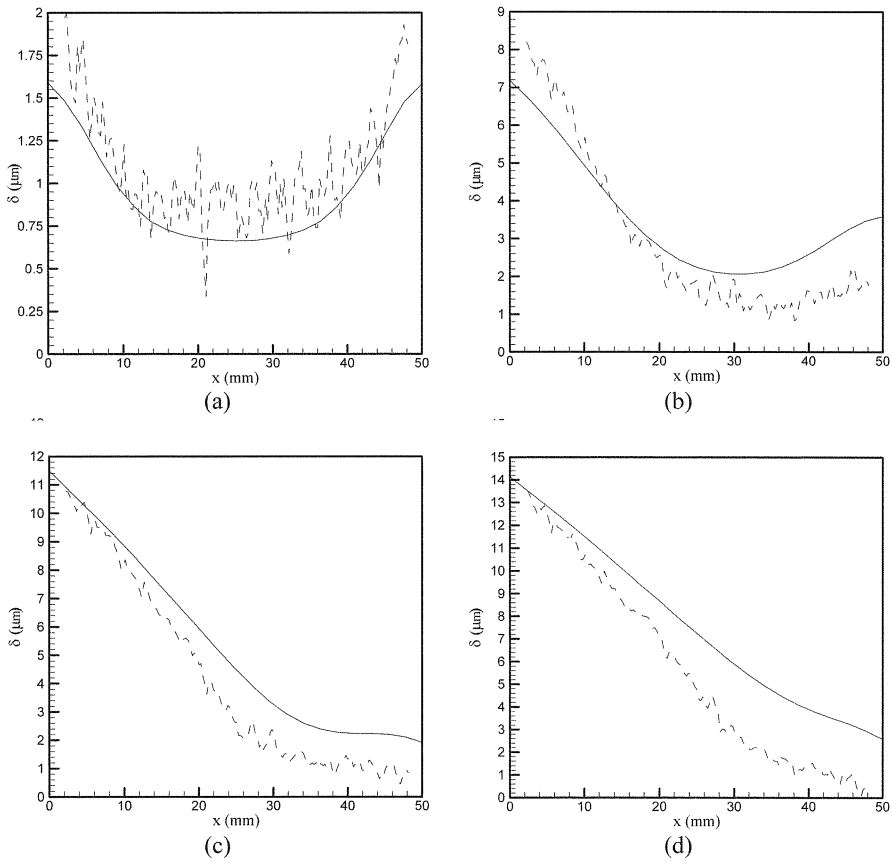
Figure 12: Load-deformation curve for non-symmetric crack growth due to a weaker element.

Figure 13: Deformation profiles at (a) load level I, (b) load level II, (c) load level III and (d) load level IV (solid lines represent numerical results).
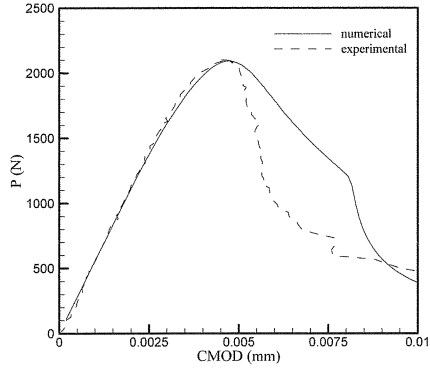
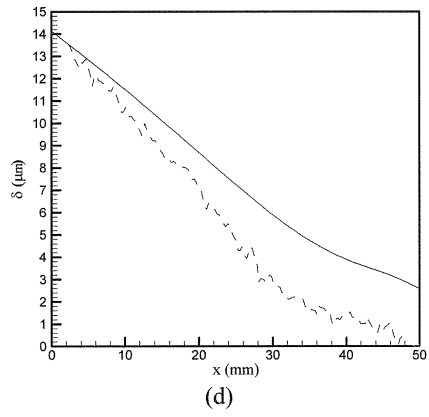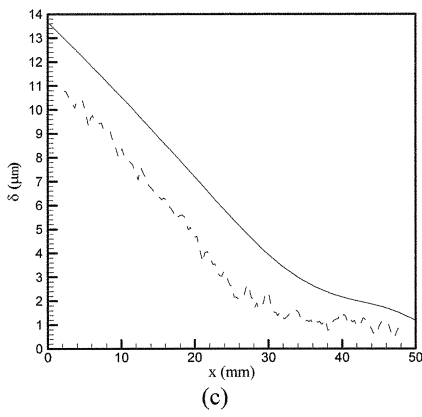*Figure 14: Load-deformation curve for DEN test with bending.*
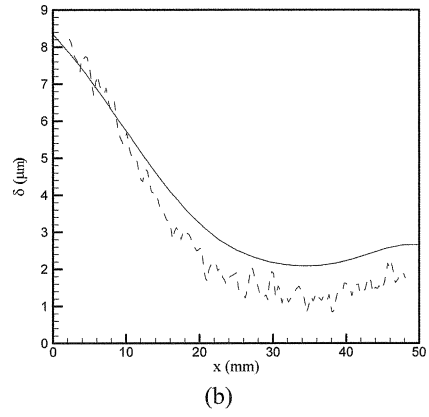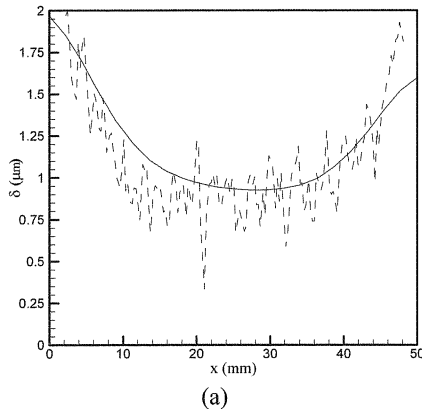

Figure 15: Deformation profiles obtained with eccentric loading for (a) load level I, (b) load level II, (c) load level III and (d) load level IV (solid lines represent numerical results).

When the deformation profiles in figure 13 are studied, the sudden drop in the load deformation curve may be explained. Clearly, in the beginning, the computed deformation profiles follow the experimentally obtained curves well. For the last load level, figure 13d, the computed deformation profile returns to a more uniform distribution. This is connected to the drop in the load-deformation curve. The drop is explained by the transition from a non-symmetric mode into a uniform pattern.

Another way to incorporate non-symmetric crack propagation is by introducing a bending component in the set-up. In this case, the force is applied with a slight eccentricity. The eccentricity of $e = 2.2$ mm is adopted and the following model parameters are used: $f_t = 7.3$ MPa, $c = 20$ MPa, $\phi = 26.35°$, $G_{fI} = 0.035$ N/mm and $G_{fII} = 0.1$ N/mm.

The load-deformation curve is shown in figure 14. Again the peak load is reproduced well. Furthermore, the drop in the load-deformation curve, already observed in figure 12, is also present and is more pronounced. The numerically obtained deformation profiles are compared with experimental results in figure 15a-d. It is clear that a non-symmetric deformation profile is obtained due to the presence of bending. For all load-levels, the computed profiles are close to the experimental curves. Even after the drop in the load-deformation curve, the computational results follow the experimental results remarkably well.

5.2 Cyclic loading

Next to the monotonically loaded specimens, cyclic loading is also studied experimentally. The numerical modelling is performed with the combined damage-plasticity model defined in section 4.3. Only non-symmetric crack growth is considered.

In a first simulation, non-symmetric crack growth is triggered by a weaker element at the right notch. The adopted model parameters are: $f_t = 6.5$ MPa, $H = 27000$ N/mm^3 and $\beta = 400$. The experimentally and numerically obtained load-deformation curves are plotted in figure 16. Obviously,
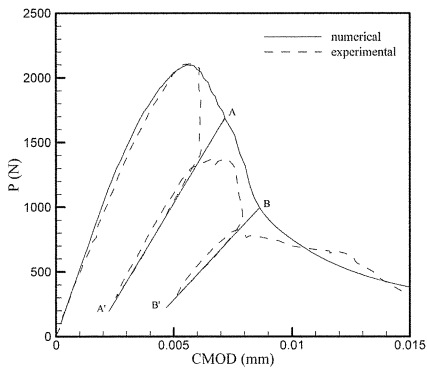

Figure 16: Comparison of experimental and numerical (with material weakness) obtained load-deformation curve for cyclic loading.
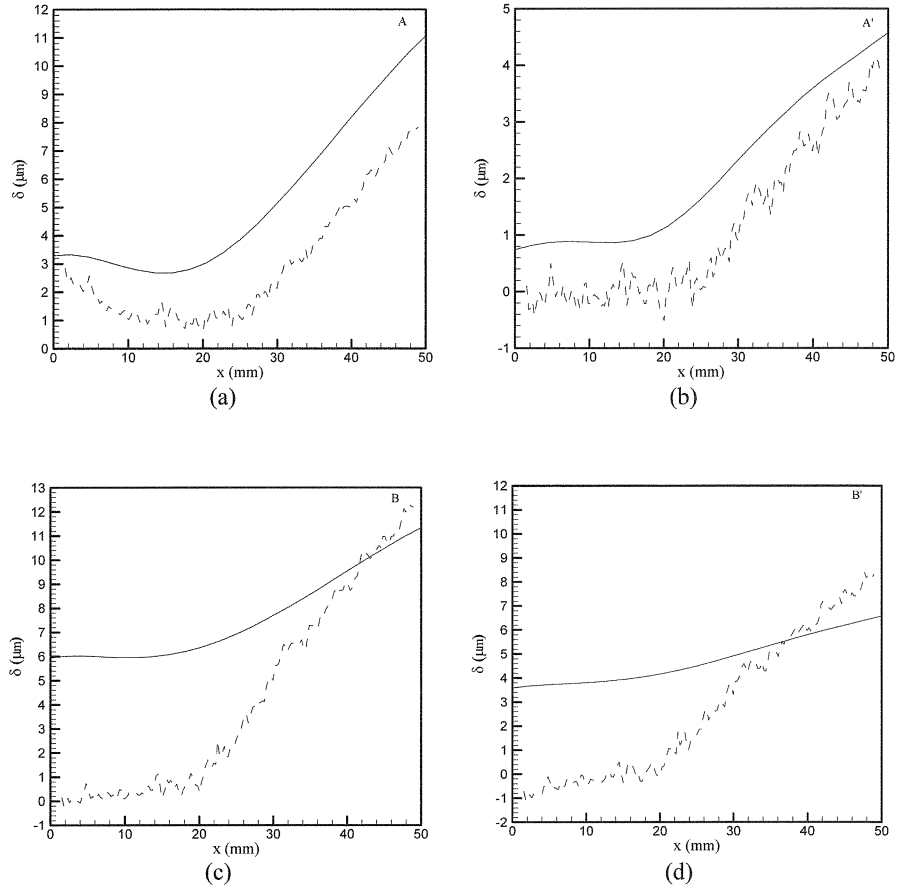
237

Figure 17: Deformation profiles for (a) begin and (b) end unloading branch 1 and (c) begin and (d) end unloading branch 2 (solid lines represent numerical results).

the proposed combined damage-plasticity model can capture the decrease of stiffness and the appearance of permanent deformations. The post peak behaviour of the numerical simulation is more ductile. The steep descent in the beginning of the post peak was not captured.

The computed deformation profiles are compared with experimental measured curves in figure 17a-d. Snapshots are taken at the beginning and the end of the unloading branches. For unloading branch 1, the deformation profiles are similar. After unloading (see figure 17b) the calculation shows permanent deformations at the left side of the specimen while the experimental deformations largely disappear. This means that during the calculation, a discontinuity is already introduced at the left side, while in reality, the behaviour is still elastic. For the second unloading branch the difference is even more pronounced.
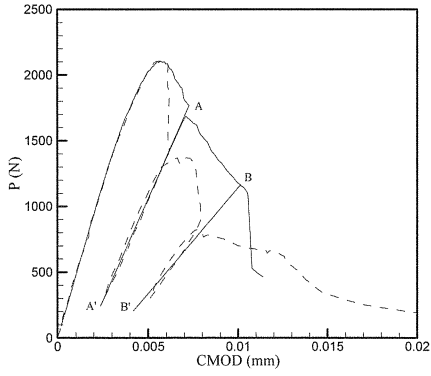
Figure 18: Comparison of experimental and numerical (with added bending) obtained load-deformation curve for cyclic loading.
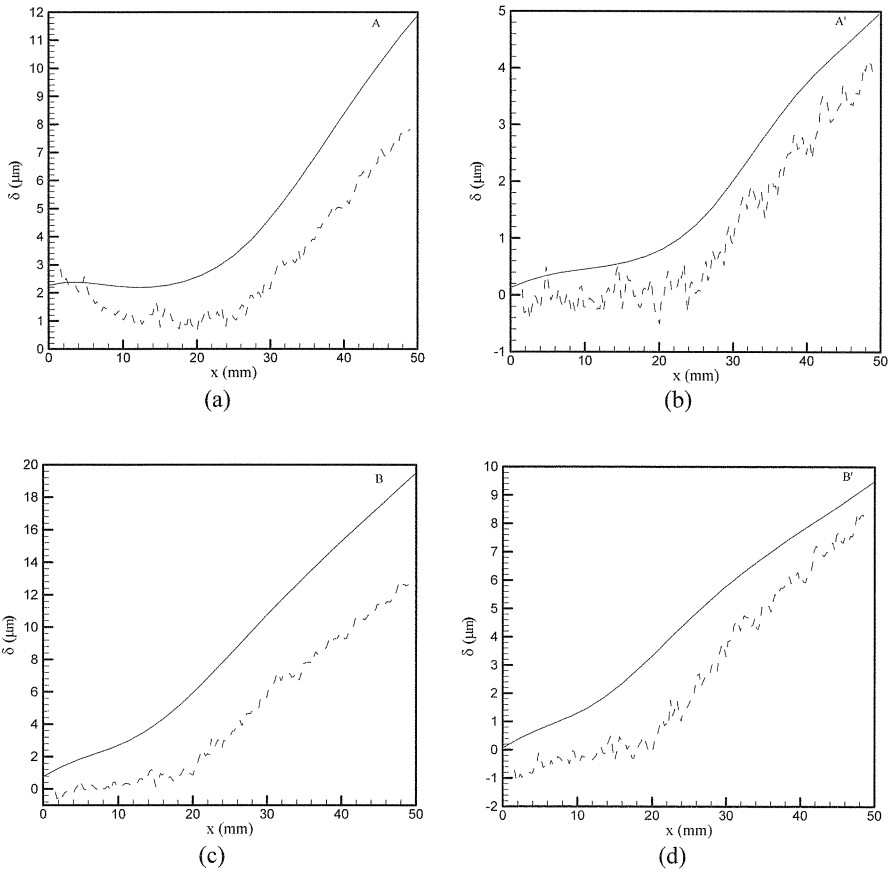

Figure 19: Deformation profiles for (a) begin and (b) end unloading branch 1 and (c) begin and (d) end unloading branch 2 (solid lines represent numerical results).

239

The same simulations are repeated for non-symmetric crack growth triggered by an additional bending moment. The adopted model parameters are: $f_t = 7.8$ MPa, $H = 27000$ N/mm^3 and $\beta = 400$. The obtained load-deformation curve is compared with the experimental value in figure 18. Again, the computed peak load is comparable with the experimental measured value, while the computed post peak behaviour is more ductile. The experimental and computed deformation profiles are compared in figure 19a-d. Compared with figure 17, the deformation profiles after unloading (figure 17b – figure 18b) are better captured when a bending moment is introduced. Furthermore, the computed deformations are higher than the measured ones.

6   Conclusions

In this paper, a combined experimental-computational study of the tensile behaviour of limestone in presented. Both monotonic as well as cyclic loading was performed. During the experiments, both global and local measurements were made. Globally, the load-deformation curve was recorded and locally, the displacement field around the crack tip was measured. It was shown that with the use of the ESPI technique, important information can be recorded. Moreover, the ESPI technique is very useful since there is no contact with the specimen, and consequently, the measurement do not interfere with the experimental process.

Measurements showed that the obtained deformations are non-symmetric. After unloading, it was shown that permanent deformations were present. For the numerical simulations, the discontinuous finite elements were used in combination with a plasticity-based and a combined damage-plasticity cohesive zone model. For the monotonic loading, the simulations were performed with the plasticity based model, while for cyclic loading the combined damage-plasticity model was used. The combined model was necessary in order to correctly capture the decrease in the unloading stiffness and the permanent deformations after unloading. However, it was shown that the experimental observations could not be captured with the numerical model and consequently, the problem must be modified. Therefore, a weaker region or an additional bending component was added. It was shown that, with the enhancement, the experiments were simulated more accurately.

This paper shows that comparing numerical simulations with experimental data should be done with great care. A fit of the simulations to the global data is not sufficient to conclude that the model can capture the real response. Local data in computations and from experiments should be compared. Consequently, the derivation of the material parameters from an experiment is not straightforward.

Acknowledgements

References

- Carol, I., Prat, P.C. and Lopez, C.M. (1997). Normal/shear cracking model: application to discrete crack analysis. *Journal of Engineering Mechanics*, 123, 765-773.
- De Proft K. (2003). A combined experimental-computational study to discrete fracture of brittle materials, Phd thesis, Vrije Universiteit Brussel.
- Simo, J.C. and Ju, J.W. (1987). Strain- and stress-based continuum damage models – I. Formulation, II. Computational aspects, *International Journal of Solids and Structures*, 23(7), 821-869.
- Wells, G.N. and Sluys, L.J. (2001). A new method for modeling cohesive cracks using finite elements. *International Journal for Numerical Methods in Engineering*, 50(12), 2667-2682.
- Wells (2001). Discontinuous modelling of strain localization and failure, Phd thesis, TU Delft.